Natural Hazards (2021) 106:1125–1147
https://doi.org/10.1007/s11069-020-04146-x

ORIGINAL PAPER

On the possibility of seismic recording of meteotsunamis

Emile A. Okal[1]

Received: 5 March 2020 / Accepted: 1 July 2020 / Published online: 15 July 2020

Abstract
We use the horizontal components of land-based seismometers in the vicinity of shorelines to apply to meteotsunamis the deconvolution algorithm introduced by Okal (Pure Appl Geophys 164:325–353, 2007) in order to recover time series of tsunami amplitudes from seismic recordings. For a selected set of seven such events recorded at 16 seismic stations, we obtain equivalent wave amplitudes and horizontal polarizations, the latter expressing the directions of particle motions at the surface of the sea. Our amplitudes are generally on the same order of magnitude as available regional records or reports, and the direction of tsunami currents is found mostly parallel to the relevant shorelines. In particular, seismic records available at three Spanish stations suggest that the unexplained waves which killed twelve people in Mostaganem, Algeria in 2007, had a meteorological origin. Our results, of an exploratory nature, suggest that seismic records could play an important role in the further understanding of the structure of meteotsunamis.

Keywords Meteotsunamis · Seismic deconvolution · Mostaganem

1 Introduction and background

This paper assesses the possibility of recording meteotsunamis on the horizontal components of land-based seismometers deployed in the immediate vicinity of the affected coastlines.

Following the 2004 Indonesian tsunami, Yuan et al. (2005) first reported the recording of tsunami waves by broadband seismic stations deployed at teleseismic distances on oceanic islands of the Indian Ocean. In very general terms, tsunami waves were found to be detectable on horizontal components in the frequency band 0.5–10 mHz and at amplitude levels suggesting ground accelerations of 1–10 μm/s^2. Similar observations were also reported qualitatively by Hanson and Bowman (2005).

In Okal (2007), we later showed that such recordings could be made worldwide at stations located within ~30 km of coastlines and that the resulting amplitudes could be quantified in the framework of Ward's (1980) representation of tsunami waves as a special branch of the free oscillations of the Earth, by simply assuming that the station

✉ Emile A. Okal
emile@earth.northwestern.edu

[1] Department of Earth and Planetary Sciences, Northwestern University, Evanston, IL 60208, USA

was actually sitting on a flat ocean floor, in the absence of the island or continent. This drastic, if not outrageous, simplification was justified by the very large wavelengths of earthquake-generated tsunamis (Rabinovich 1997). In this framework, and following Gilbert (1980), a horizontal seismometer responds not only to the horizontal acceleration of the solid Earth, but also to a component of tilt and to a change in the gravitational potential induced by the Earth's oscillation. In the case of a standard Rayleigh mode, those two corrections can alter the precise quantification of its recorded amplitude by at most 10%; by contrast, in the case of tsunami modes, their effect can reach 1.5 orders of magnitude (Okal 2007), thus greatly amplifying the recording of the minute horizontal component of the continuation of the tsunami eigenfunction into a solid Earth of finite rigidity.

Okal (2007) went on to define a "Gilbert Response Function," $GRF(\omega)$, as the ratio, at each angular frequency ω, of the apparent horizontal displacement u_x^{app} recorded by the instrument to the vertical amplitude η of the tsunami at the surface of the ocean:

$$GRF(\omega) = \frac{u_x^{app}}{\eta} = l\,y_3 - \frac{1}{C\,\omega}(g y_1 - y_5) \tag{1}$$

where, in the notation of Saito (1967), y_1 and $l\,y_3$ are the vertical and horizontal components of ground motion at the bottom of the ocean for a tsunami mode of angular degree l, and y_5 is the perturbation of the Earth's gravitational potential accompanying the oscillation of the mode (for a normalized surface amplitude of 1 unit); C is the phase velocity of the tsunami mode and g the acceleration of gravity. The Gilbert Response Function can then be regarded as a frequency-dependent transfer function, to be combined with the classical instrument response, in order to transform the seismometer into a "tsunameter" measuring the amplitude η of the tsunami on the high seas. Using this approach, and for six earthquake-generated tsunamis, Okal (2007) recomputed the seismic moment of their parent earthquakes generally within a factor of 2 of the published Harvard Centroid Moment Tensors (now GlobalCMT) solutions (Dziewonski et al. 1981; Ekström et al. 2012).

As discussed in the Appendix of Okal (2007), the function $GRF(\omega)$ is essentially independent of the depth H of the water column. This remarkable property was later extended to the case of a very shallow basin by Paris et al. (2019), who proposed the general expression

$$\log_{10} GRF(\omega) = -2 \log_{10} f - 1.317 \tag{2}$$

where $f = \omega/2\pi$ is in millihertz, with $0.1 \leq f \leq 10$ mHz, and for depths H ranging from 100 m to 4 km. They then used a seismic record in the near field to reconstruct a water amplitude $\eta \approx 1.9$ m in the case of the landslide-generated tsunami of June 17, 2017, at Karrat Fjord, Greenland. We emphasize that, even though the theoretical justification of the independence of GRF on H was given by Okal (2007) under the shallow water approximation, the regression (2) was obtained by Paris et al. (2019) using fully dispersed normal mode theory. Note finally that seismic recordings of local tsunamis had also been made, but only qualitatively, at an epicentral distance of 21 km during the Stromboli tsunami generated by a volcanic landslide at La Sciara (La Rocca et al. 2004).

In this context, the purpose of this paper is to use seismic recordings in the near field to reconstruct wave amplitudes for a sample of meteotsunamis having occurred in the past 15 years.

2 Dataset and methods

We refer to Rabinovich (2020) for an extensive compilation of meteotsunamis documented worldwide in the past 25 years. We list in Table 1 a selection of events from that study; it is not meant to be exhaustive, but rather to offer, in the present exploratory study, a dataset allowing to test the concept of the quantitative seismic recording of meteotsunamis. We add two events (**F** and **G**) not included in Rabinovich (2020), as they provide a unique perspective. Figure 1 is a world map of the events selected.

For each meteotsunami, we identified appropriate seismic stations, located within a few km of the affected coastline. Given the seismically low frequencies of meteotsunamis, we targeted coarsely sampled channels, typically the "L" bands sampled at 1 Hz, but occasionally had to work with "B" channels sampled at 20 Hz, and exceptionally "H" bands sampled at 100 Hz. Horizontal seismograms were then processed through a classical spectrogram analysis to extract time and frequency windows containing the tsunami signal. We then deconvolved the instrument response and the Gilbert Response Function (Eq. 2) in the 0.1–10 mHz band, to construct equivalent time series of the surface amplitude of the tsunami wave, $\eta(t)$, and a classical particle motion algorithm was used to infer its horizontal polarization and hence the azimuth of the tsunami wave in the vicinity of the station. We retain and list in Table 1 the maximum zero-to-peak amplitude η_{max} of the rotated time series and the dominant period in its spectrum.

3 Results

3.1 Event A: Menorca, Spain, June 15, 2006

We first consider this "*rissaga*" event, which provided the cleanest and sharpest seismic recording of a meteotsunami. As documented by Monserrat et al. (2006), Jansà et al. (2007) and Vilibić et al. (2008), it resulted in catastrophic flooding with run-up reaching 5 m in Ciutadella Harbor on the western coast of Menorca. The closest available seismic record is at Mahón (MAHO), on the eastern coast, at a distance of $\sim$ 40 km (Fig. 2).

The tsunami is clearly identified on the raw seismograms at MAHO, with impulsive onsets at 19:14:30 GMT. Spectrograms are shown in Fig. 2. The deconvolved η time series, as shown in Fig. 3, reach an amplitude of 2.4 m, polarized in the N320°E azimuth, which is consistent with the orientation of the local inlet at Mahón. This amplitude is smaller than reported at Ciutadella (4–6 m), but remains on the same order of magnitude. The dominant period (30 mn) is also significantly longer than reported at Ciutadella (10.5 mn); such differences in amplitude and period between the two locations reflect the nonlinear response of two inlets with differing shapes and dimensions.

3.2 Event B: Mediterranean Sea, June 22–27, 2014

We next analyze this remarkable phenomenon, which involved most of the Mediterranean Sea (Fig. 4), from Menorca in the Balearic Islands to the Aegean coast of Turkey, and into the Black Sea (Šepić et al. 2015). Figure 5 presents a summary of deconvolved particle motions obtained, from east to west, at Mahón, Menorca; Ston,

Table 1 List of events and records used in this study

Event	Date	Region	Index [*Rabinovich,* 2020]	Station				Equivalent η_{max} (cm)	Best Azimuth (°)	Dominant Period (s)
				Name	Code	Lat. (°N)	Lon. (° E)			
			Events listed by Rabinovich [2020]							
A	15 JUN (166) 2006	Menorca, Spain	10	Mahón	MAHO	39.90	4.27	239	320	1796
B	22−27 JUN (173−178) 2014	Mediterranean	34	Mahón	MAHO	39.90	4.27	6.6	216	2149
				Ston	STON	42.87	17.70	517	271	1645
				Podgorica	PDG	42.43	19.26	4.3	304	2081
				Ag. Paraskevi	PRK	39.25	26.27	28.4	*	2313
				Dikili	DKL	39.07	26.91	126	224	1997
				Târguşor	TIRR	44.46	28.41	20.6	327	1846
C	13 JUN (164) 2013	Atlantic Sea Coast, USA	31	Falmouth	M65A	41.56	-70.65	58.4	266	2114
				Hydrophone 02	W02H	39.56	-70.85	18.0		2675
				Hydrophone 04	W04H	39.43	-71.48	29.7		3543
				Dart Sensor	44402	39.29	-70.64	3.3		3091
				Tide Gauge	WHOI	41.53	-70.67	28.		3178
D	30−31 MAR (089−090) 2007	Korea	13	Jeju Island	JJU	33.43	126.55	87	195	3084
				Incheon	INCN	37.48	126.62	11		2341
E	13 APR (103) 2018	Lake Michigan, USA	45	Ryerson Woods	L44A	42.18	-87.91	29.5	238	1489
				Eau Claire	L46A	42.01	-86.30	14.6	228	1928
			Additional Events							
F	26−29 DEC (361−364) 2004	Atlantic Sea Coast, USA		New Hope	NHSC	33.11	-80.18	140	236	1820
G	03 AUG (215) 2007	Mostaganem, Algeria		Cartagena	CART	37.59	-1.00	11.1	273	1365
				Melilla	MELI	35.29	-2.94	23.8	223	2280
				Mahón	MAHO	39.90	4.27	5.8	302	1771

* Variable; see text.

*Variable; see text

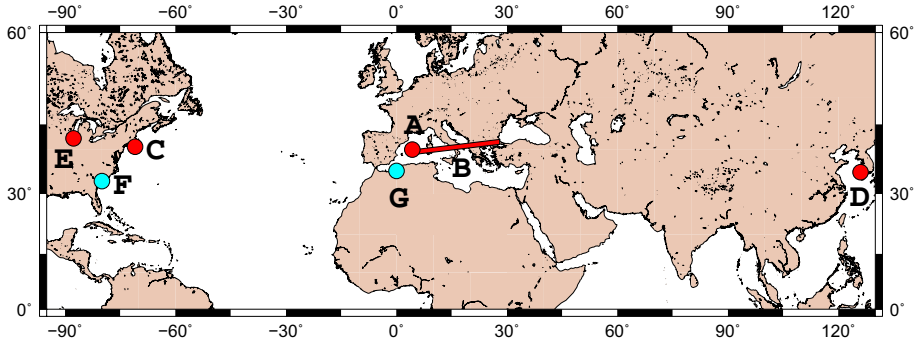

Fig. 1 World map of the seven events studied, as referenced in the text and Table 1. The red symbols identify those listed by Rabinovich (2020), including Event **B**, which stretched over most of the Mediterranean Sea. The blue symbols (Events **F** and **G**) are additional ones

Croatia; Podgorica, Montenegro; Târguşor, Romania; Ag. Paraskevi (Lesvos), Greece; and Dikili, Turkey.

We note significant variations in deconvolved amplitudes and in their polarization. The former generally agree with the reports by Rabinovich (2020), with the strongest waves observed in the Adriatic (STON). They remain centimetric in Mahón, where the polarization is this time NNE–SSW, presumably reflecting the absence of an efficient resonance of the inlet, which may due to longer periods than during Event **A.** By contrast, the exceptional amplitudes deconvolved at Ston (reaching 5 m) and the pure EW polarization could be attributed to resonance in the channel featuring an extremely complex geometry immediately off the recording station. At Podgorica, located about 30 km inland, and despite meager amplitudes, the polarization follows the general direction of the coastline of the Adriatic Sea; it could also fit the orientation of nearby Lake Skadar, suggesting a possible seiching, but the depth of the lake is poorly known and this interpretation remains speculative. Similarly, at Târguşor, the polarization of the deconvolved wavefield follows the local coastline of the Black Sea. At Dikili, we reconstruct metric amplitudes, in agreement with the reports by Rabinovich (2020), with a NE–SW polarization coinciding with the general orientation of the channel to the east of the island of Lesvos.

Finally, we compare the recordings at Dikili with those at the nearby Greek Station Ag. Paraskevi, a mere 50 km away on the island of Lesvos (Fig. 4b). While the polarization at Dikili is remarkably homogeneous, the results on Lesvos are clearly bimodal, with the first part of the deconvolved time series (from 02:05 to 09:40 on June 27, in red in Fig. 5) oriented N248°E, only 23° from its counterpart at Dikili, but the later part (from 09:40 on, in blue) rotated an additional 45°. This indicates that the station at Ag. Paraskevi records a tsunami wavefield composed of two arrivals at different azimuths and separated by about 7.5 h.

3.3 Event C: Northeast U.S. Atlantic Coast, June 13, 2013

This event resulted from a so-called *derecho* weather system (Šepić and Rabinovich 2014) which affected the eastern seaboard of the USA, from North Carolina to Massachusetts. We refer to Bailey et al. (2014) and Wertman et al. (2014) for a complete description and

Fig. 2 *Top:* Map of Menorca, Balearic Islands, showing the locations of Ciutadella where maximum run-up was observed during Event **A**, and of the recording station Mahón (MAHO). Isobaths are contoured at 100-m intervals to 1000 m (green) and at 500 m deeper (blue). *Center:* Time series (top) and spectrogram (bottom) for the north–south seismic record at Station MAHO. The time series is a raw seismogram, the vertical scale being arbitrary digital units. Each pixel in the spectrogram represents the spectral amplitude at the relevant frequency in a window of length $\Delta t = 1500$ s, moving across the time series in steps $\delta t = 25$ s, color-coded according to the scale at right, in decibels relative to the strongest pixel. *Bottom:* Same as center for the east–west component

to Knight et al. (2013) for a modeling of its generation by Proudman resonance (Proudman 1929) on the continental shelf.

We examine here the seismic records at Station M65A (Falmouth, Massachusetts) and then operated as part of the Transportable Array.[1] Figure 6a shows a 24-h window of the raw east–west LHE channel (sampled at 1 Hz), with the deconvolved equivalent wave amplitude $\eta\,(t)$ shown in Fig. 6b. Note that the peak-to-peak amplitude (114 cm) is about double that recorded on the tidal gauge station at Woods Hole, less than 5 km away, as described by Dusek et al. (2019) and confirmed in Fig. 7d, but more in line with news reports quoted by Rabinovich (2020) of up to 1.5 m (5 ft.; probably peak to trough) at various locations of the eastern seashore. This discrepancy may be attributable to a difference in instrumentation, tidal gauges often featuring by design high-pass mechanical filters and most importantly, a very coarse sampling rate, in this case 1 sample every 6 minutes, resulting in a Nyquist frequency of 1.4 mHz.

There is also some discrepancy in timing between the arrivals of the tsunami on the deconvolved M65A time series (around 11,000 s into the time series, or ~15:10 GMT) and on the Woods Hole tidal gauge (not before 18:20 with a sharp onset at 19:30; Fig. 7d). However, the spectrogram of the time series shows that the maximum energy does arrive at M65A around 18:40 (right arrow in Fig. 6c). This timing difference may illustrate the fact that the tidal gauge records the arrival at the coast, following passage by the tsunami over the extremely shallow waters (< 20 m) between Woods Hole and Martha's Vineyard, whereas the deconvolution has the effect of a filter averaging the tsunami field over a greater area. This interpretation is supported by the polarization of the deconvolved field, which is perfectly EW, reflecting the general direction of the coasts of Cape Cod, Martha's Vineyard and Nantucket, rather than the direction of the straits immediately adjacent to the receiver (Fig. 6e).

We also examined the waveforms recorded by two hydrophones: W02H and W04H, shown as triangles in Fig. 7, and deployed at the time at the toe of the continental shelf, respectively, 223 km and 247 km south of M65A. Figure 7 presents equivalent sea surface amplitudes $\eta\,(t)$ after deconvolving the instrument response in the same 0.1–10 mHz band. The smaller amplitudes reflect the faltering of the meteotsunami, generated in shallow water, as it penetrates the deeper ocean, an illustration of Green's law (Green 1838; Synolakis 1991). While the waveform at W04H is generally comparable to the deconvolved η at M65A, the time series at W02H is much simpler, consisting of a single pulse. We have no explanation for this discrepancy, especially since the two hydrophones lay only 56 km apart at essentially identical depths (2386 and 2288 m, respectively). Slightly farther south, the meteotsunami was also recorded by DART station 44402 (Rabinovich 2020). We use the 15-s fine-resolution DART time series (at the time, unavailable to Wertman et al. (2014)), which we also present in Fig. 7 after band-pass filtering between 0.1 and 10 mHz. While its

[1] We note that even though Wertman et al. (2014) used the auxiliary pressure channels at stations of the Transportable Array to study the derecho, they did not search the seismic channels for any signals of the tsunami.

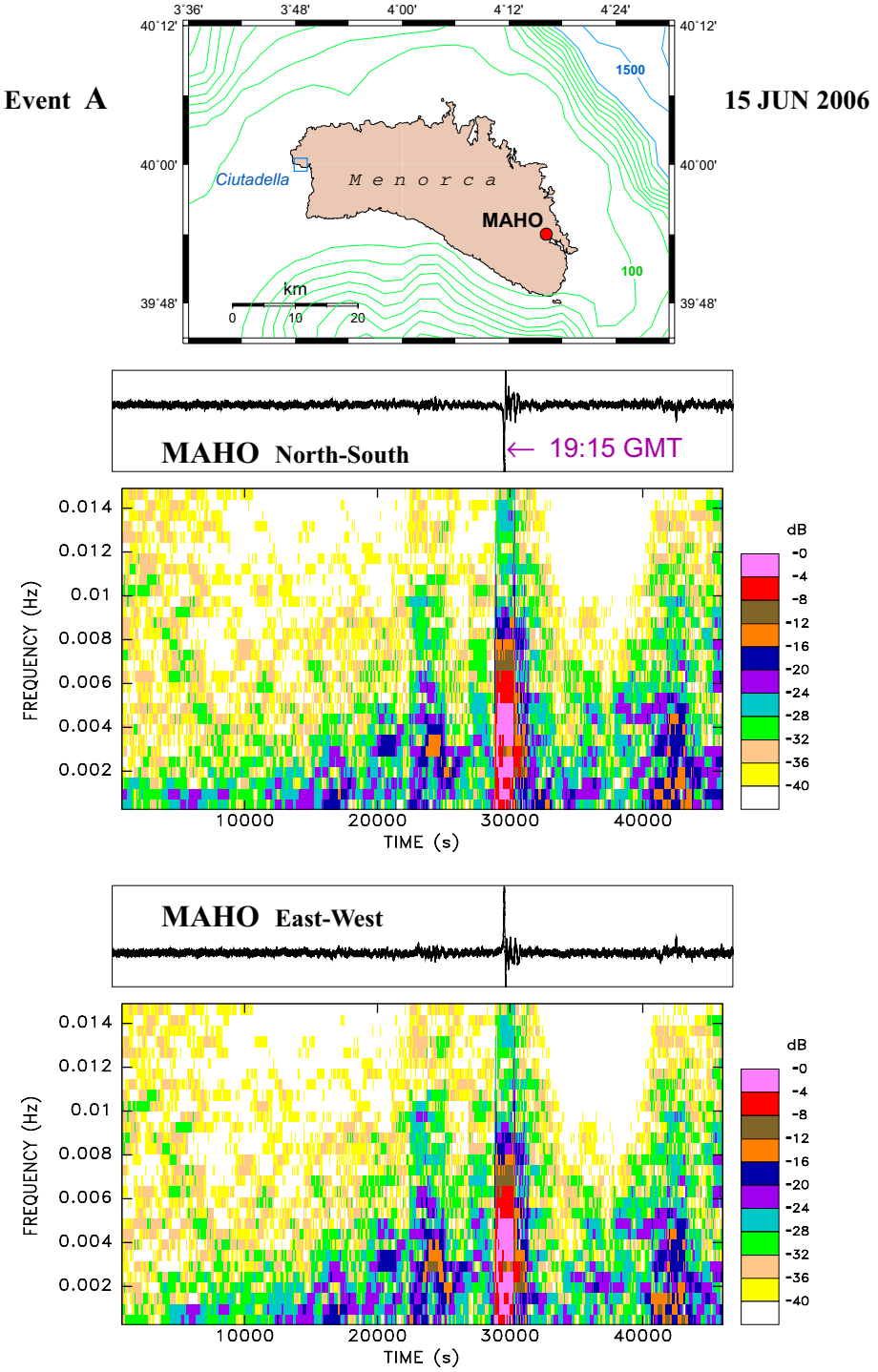
Event A
15 JUN 2006
3°36'
3°48'
4°00'
4°12'
4°24'
40°12'
40°00'
39°48'
1500
100
Menorca
Ciutadella
MAHO
km
0
10
20
MAHO North-South
← 19:15 GMT
FREQUENCY (Hz)
0.014
0.012
0.01
0.008
0.006
0.004
0.002
10000
20000
30000
40000
TIME (s)
dB
-0
-4
-8
-12
-16
-20
-24
-28
-32
-36
-40
MAHO East-West

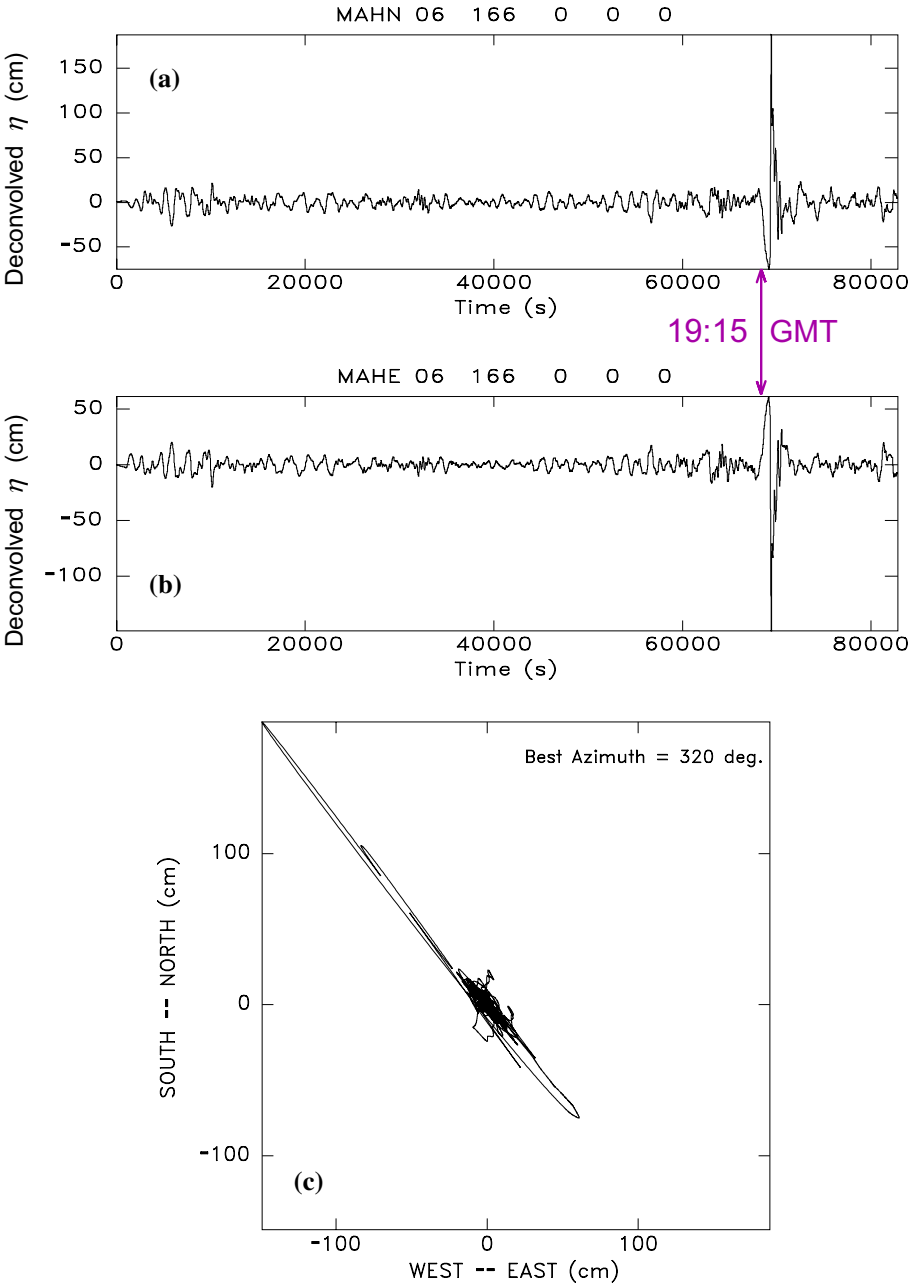

Fig. 3 **a** Equivalent wave amplitude η for Event **A** obtained from the NS seismogram at Mahón, by deconvolving the instrument response and the Gilbert Response Function *GRF*. **b** Same as (**a**) for the EW component. **c** Two-dimensional horizontal particle motion obtained from the time series in (**a**) and (**b**); the azimuth of the best fitting regression is shown

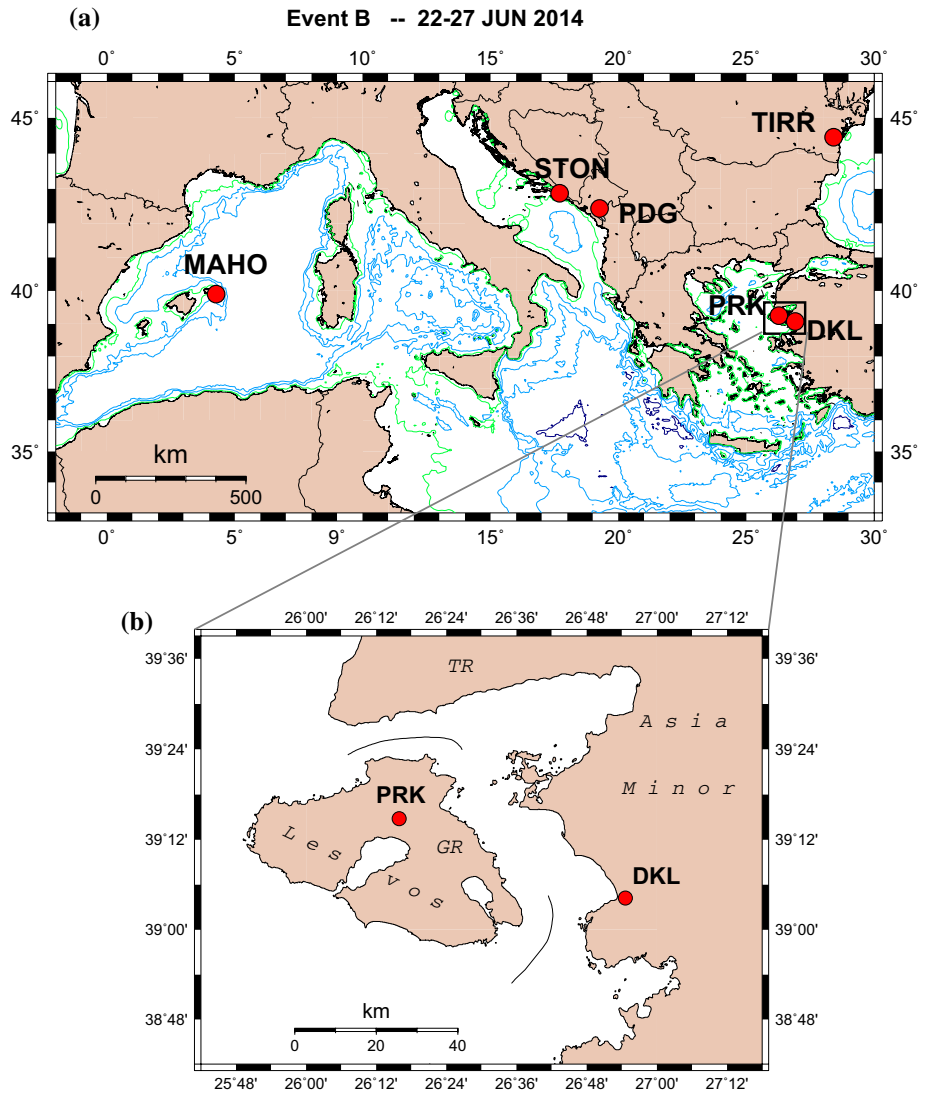

Fig. 4 **a** Map of the stations used for Event **B**, the 2013 trans-Mediterranean meteotsunami. Isobaths are at 100 m (green) and then every 1000 m (blue). **b** Close-up of main map in the eastern Aegean Sea, showing the stations Agia Paraskevi (PRK) on Lesvos (Greece) and Dikili (DKL) on the Asia Minor coast of Turkey

waveform is similar to that recorded at W02H (with the addition of a second arrival ~3.5 hr after the main one), the difference in amplitude remains unexplained, given the distance of only 20 km separating the two stations and again the similar depth of the sensors (2539 m at the DART location); this casts some doubt on the instrumental response of the sensors at W02H and W04H.

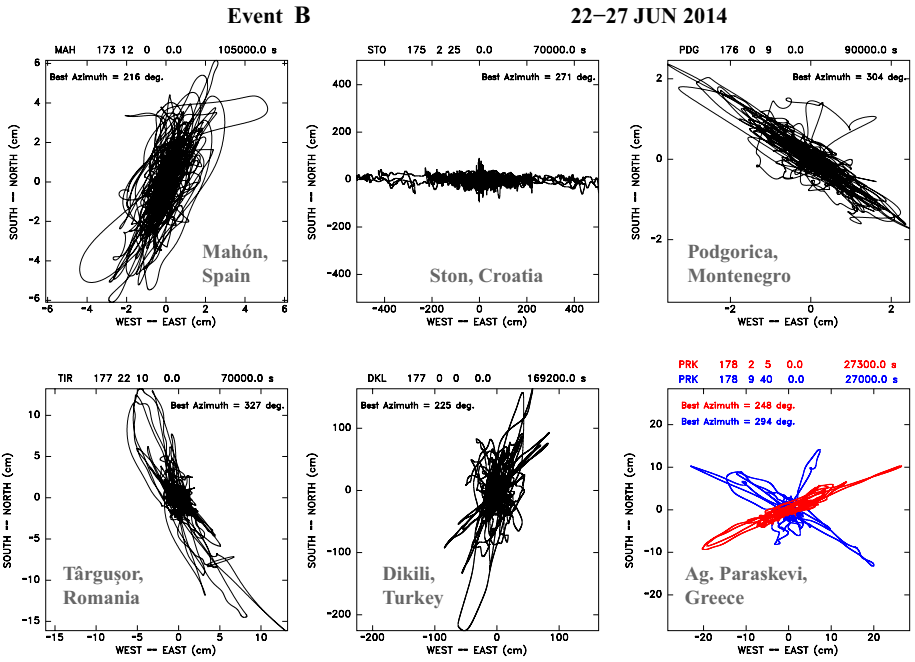

Fig. 5 Horizontal particle motions of deconvolved time series η at six stations in the Mediterranean Basin during Event **B**. In the case of Agia Paraskevi (PRK), the time series is split between its initial (red) and final (blue) phases. See text for details

3.4 Event D: Korea, March 30–31, 2007

The East China Sea (Western Sea in Korean) is a large body of very shallow water rarely exceeding 100 m in depth, with large sections shallower than 50 m (Fig. 8a), thus favoring the development of meteotsunamis through Proudman resonance. The 2007 event, described in detail by Cho et al. (2013) and Choi et al. (2014), generated waves of ~2 m on the Korean coast where it killed four people and wrought considerable damage.

The tsunami was well recorded at station JJU on Jeju Island. Figure 9a presents the raw north–south seismogram at JJU and the corresponding spectrogram, showing strong energy over a ~10-h-long window starting around 19:00 GMT on March 30. Figure 8b shows a strong north–south polarization of the deconvolved wave amplitude time series, illustrating the arrival of the tsunami from the northern part of the East China Sea, as modeled by Choi et al. (2014).

In addition, we examined the records at Incheon (INCN), a station of the global seismic network located 450 km to the north. As shown in Fig. 9b, the tsunami is also present, but arrives about 6 h earlier; note that the lower-frequency character of the spectrum is probably due to a difference in instrumentation (STS-1 *vs.* STS-2). This time shift suggests a propagation at ~21 m/s, typical of tsunami celerities in a basin of depth 45 m under the shallow water approximation.

An interesting aspect of the INCN records is that their polarization cannot be resolved (Fig. 9b). This probably reflects the complexity of the coastlines in Incheon Bay, which

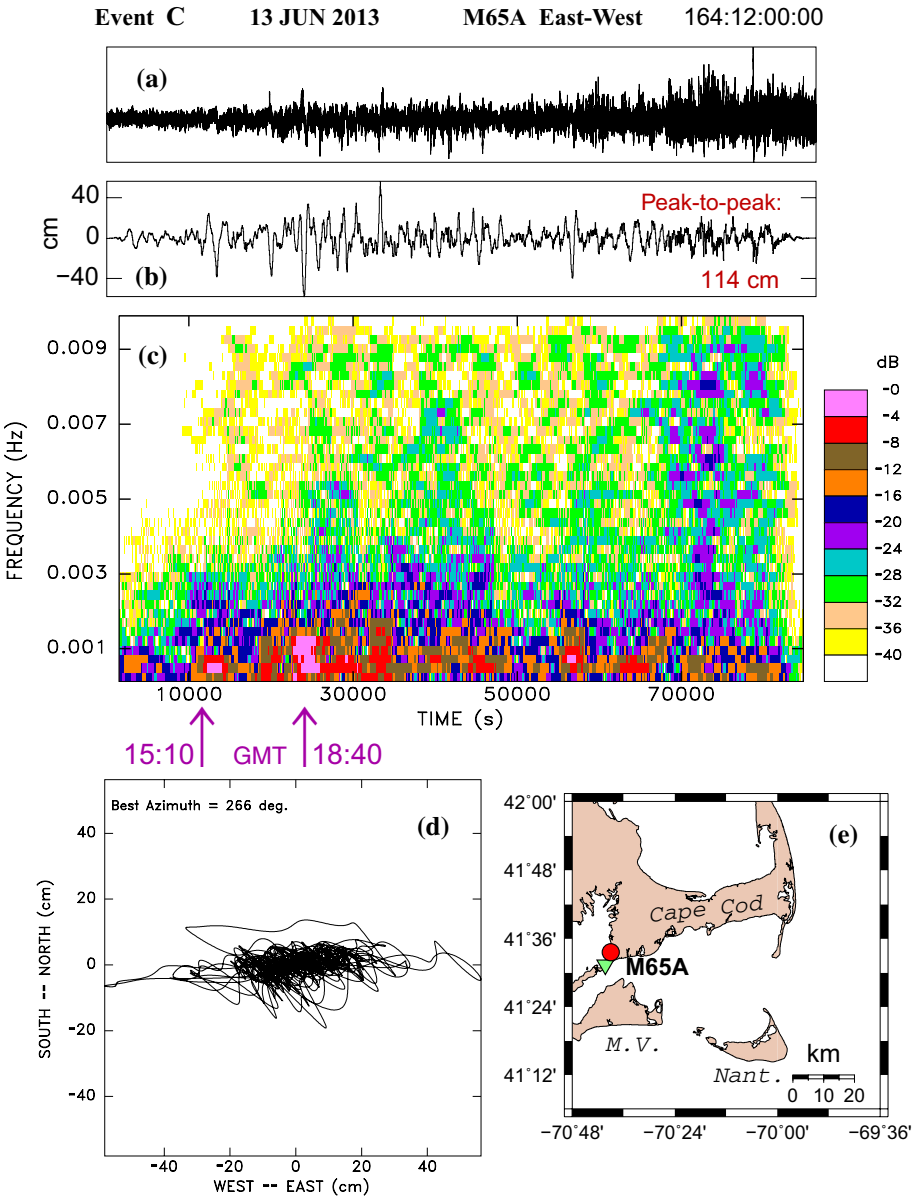

Fig. 6 **a** East–west raw seismogram at Falmouth (M65A) during the 2013 Atlantic meteotsunami. The time series starts at 12:00 on June 13. **b** Equivalent η times series, deconvolved from (**a**). **c** Spectrogram of (**a**); note maximum energy arriving around 18:40 GMT (right arrow). **d** Horizontal particle motion combining (**b**) and similar NS trace. **e** Close-up location map for Station M65A, with offshore islands (Martha's Vineyard and Nantucket); the inverted triangle shows the location of the tidal gauge in Woods Hole Harbor

is strewn with multiple islands, coves and headlands. By contrast, the coastline of Jeju, a young volcanic island, is more regular. This observation illustrates the possible limitations of the use of seismic stations for the recording of meteotsunamis in the presence of extremely irregular coastlines.

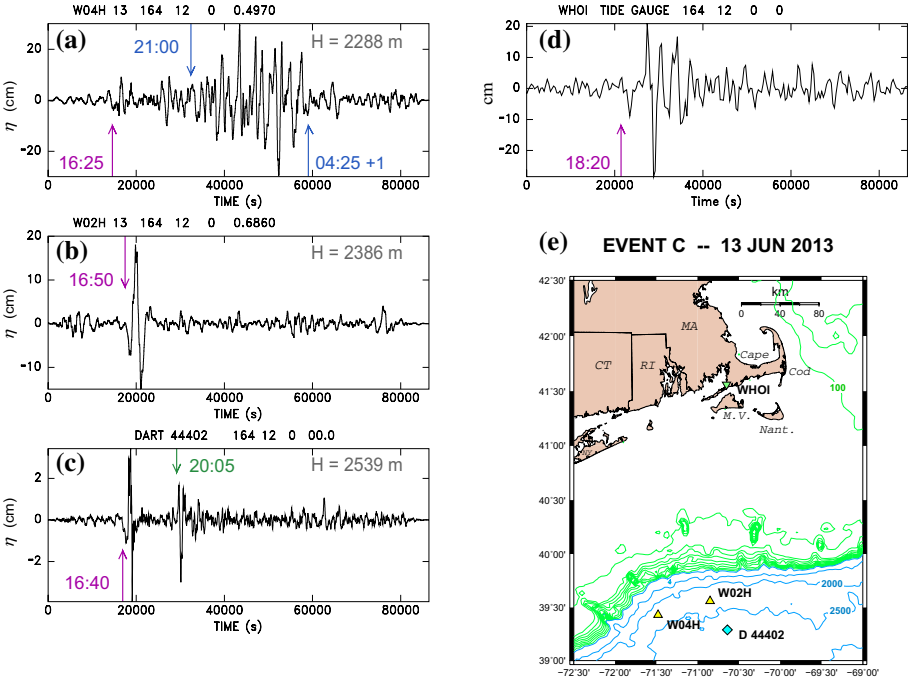

Fig. 7 *Left:* Equivalent wave amplitudes η recorded during Event **C** at ocean-bottom hydrophones W04H (**a**), W02H (**b**), plotted after correction for instrument response, and at the DART station 44402 (**c**) . *Right:* (**d**) Tidal gauge record at Woods Hole Harbor, high-pass filtered at 0.1 mHz. **e** Location map for hydrophones and DART sensor used in this study. Isobaths at 100-m intervals (green) and 500 m (blue) below 1000 m. Colored arrows show arrivals described in text; all time stamps are in universal time (GMT)

3.5 Event E: Lake Michigan, USA, April 13, 2018

This event is interesting as it took place in the general area of the famous meteotsunami of June 26, 1954, which killed at least seven people in Chicago, and which Ewing et al. (1954) immediately recognized as a case of Proudman resonance, later modeled by Platzman (1958) and more recently Bechle and Wu (2014).

The 2018 tsunami ran up ~2 m on the eastern (Michigan) side of the lake, with substantial damage in the area of Ludington, Michigan (Anderson and Mann 2019). We were able to obtain seismic signals at two stations inherited from the Transportable Array, L44A at Ryerson Woods, Illinois, and L46A at Eau Claire, Michigan (Fig. 10). Deconvolved amplitudes reach ~30 cm at L44A, but only half as much at L46A, which is double the distance from the shore. The polarization of the deconvolved time series is in both cases NE–SW, even though the relevant shorelines are oriented ~50° apart, suggesting that the direction of the tsunami in the lake is, in this instance, controlled by the weather system, rather than by interaction with specific beaches.

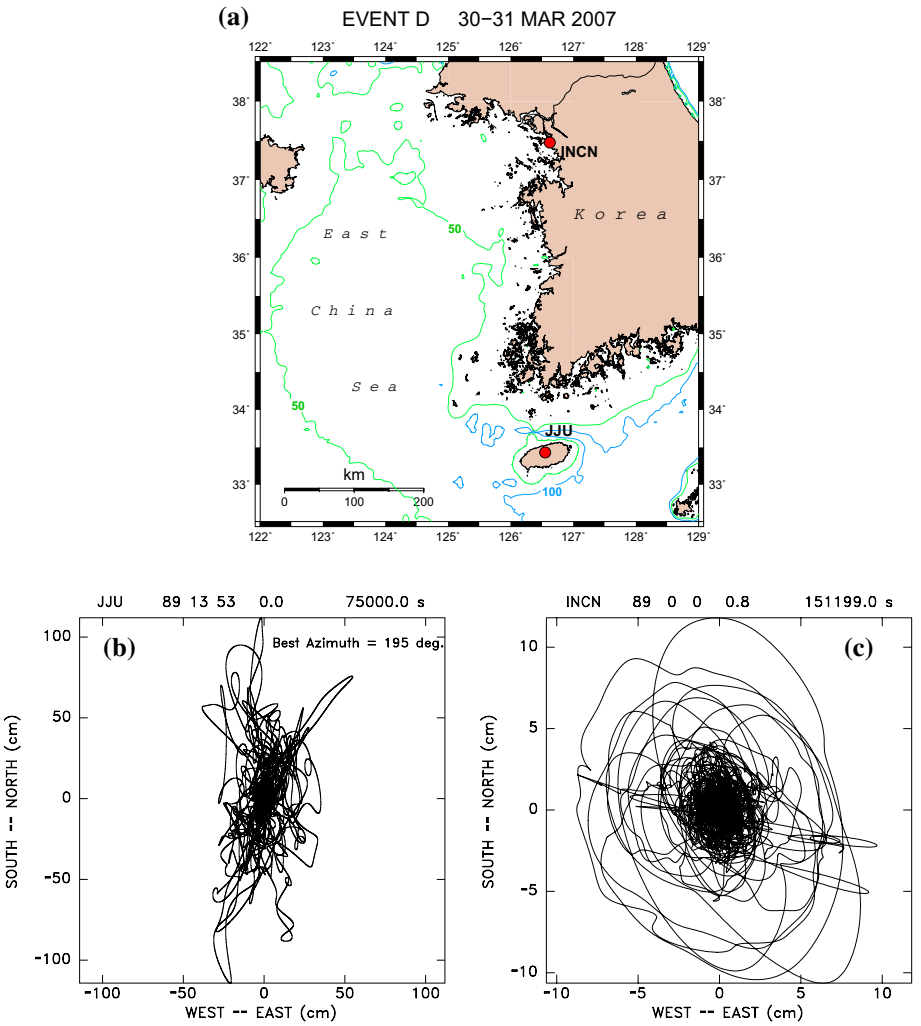

Fig. 8 **a** Location map of stations JJU (Jeju Island) and INCN (Incheon), used in the study of Event **D**. **b** Horizontal particle motion deconvolved from seismograms at JJU. **c** Same as (b) for Station INCN; note that the wavefield is not clearly polarized

3.6 Event F: Atlantic Seaboard, December 26–29, 2004

In their overview of meteotsunamis, Rabinovich and Šepić (2016) describe the fascinating coincidence, on tidal gauge records of the Atlantic coast of North America, of a local meteotsunami and of the distant Sumatra–Andaman tsunami, hitting North America after propagating some 32 h through the Indian and Atlantic Oceans. In their Fig. 4, they noted the fundamental difference in moveout of the two arrivals across the line of gauges, with the meteotsunami propagating slowly northeastward, and the Sumatra tsunami practically everywhere in phase, its wave front parallel to the coastline.

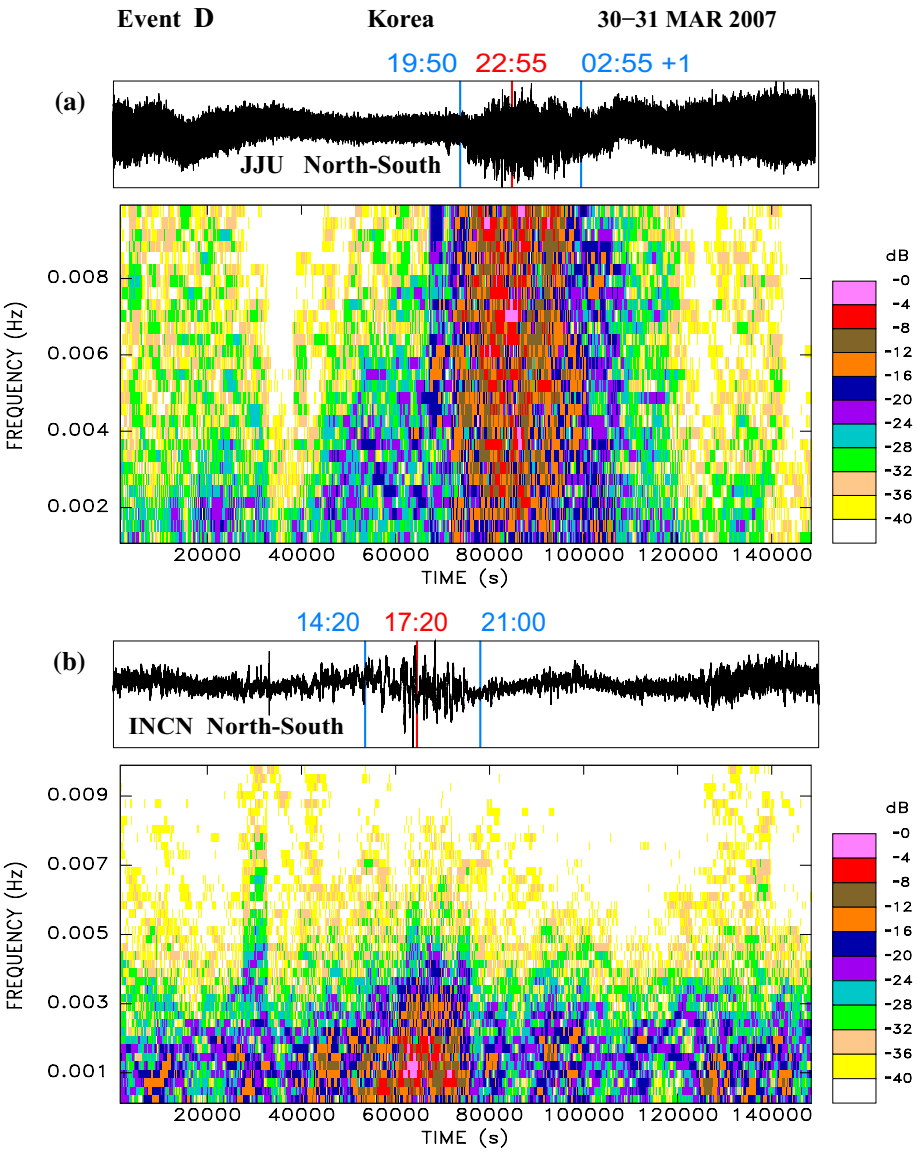

Fig. 9 Spectrograms of the horizontal seismograms at JJU *(top)* and INCN *(Bottom)* for Event **D**. Note the earlier arrival and the lower-frequency spectrum at Incheon. The blue vertical bars delineate the windows of passage of the meteotsunami and the red ones the time of maximum power; all times are GMT on March 30

Only one broadband seismic station was available for study, New Hope, South Carolina (NHS), ~40 km NNW of Charleston (Fig. 11a). Long-period oscillations are prominent in the deconvolved wave amplitude, emphasized in red in Fig. 11b, starting around 07:00 on December 26 (Julian day 361) (the shorter-period oscillations before that are meaningless since they result from deconvolving the tsunami correction *GRF* from a train of seismic waves from the Sumatra earthquake). Figure 11c documents a NE–SW polarization of the

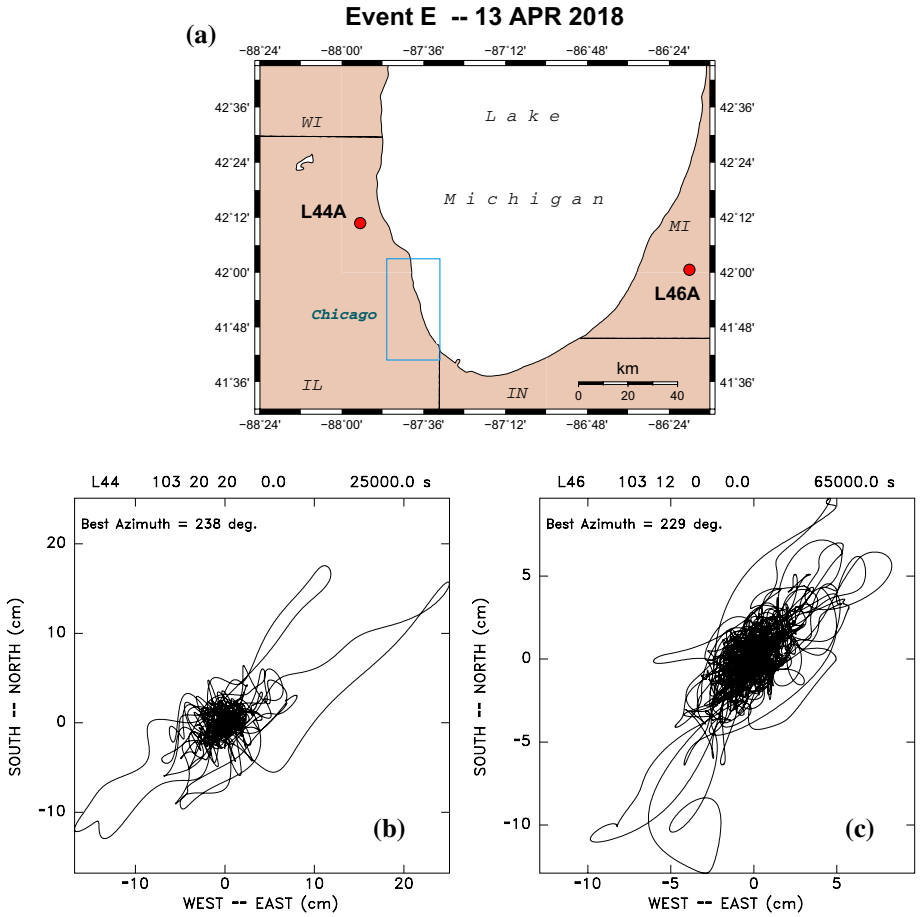

Fig. 10 **a** Location map of the two stations used for the 2018 Lake Michigan meteotsunami (Event **E**). The city of Chicago is sketched as the blue rectangle. **b** Horizontal particle motion deconvolved at Station L44A. **c** Same as (**b**) for Station L46A; note the similar orientations of the polarizations

corresponding (red) deconvolved traces, well correlated with the direction of the seaboard. In Frame (*d*), we similarly process a later window of the η time series and find a very similar polarization, indicating that the Sumatra tsunami does not contribute to them. This is in agreement with the profile of tidal gauge records shown in Fig. 4 of Rabinovich and Šepić (2016), which documents a minimum amplitude for the Sumatra tsunami at the relevant latitude, more specifically at South Capers (NOAA Station 8664941; their number 19), only 52 km away from NHS. This situation can be explained by the extensive continental shelf facing South Carolina, which absorbs the self-contained distal Sumatra tsunami, while sustaining the Proudman resonance forcing the local meteotsunami.

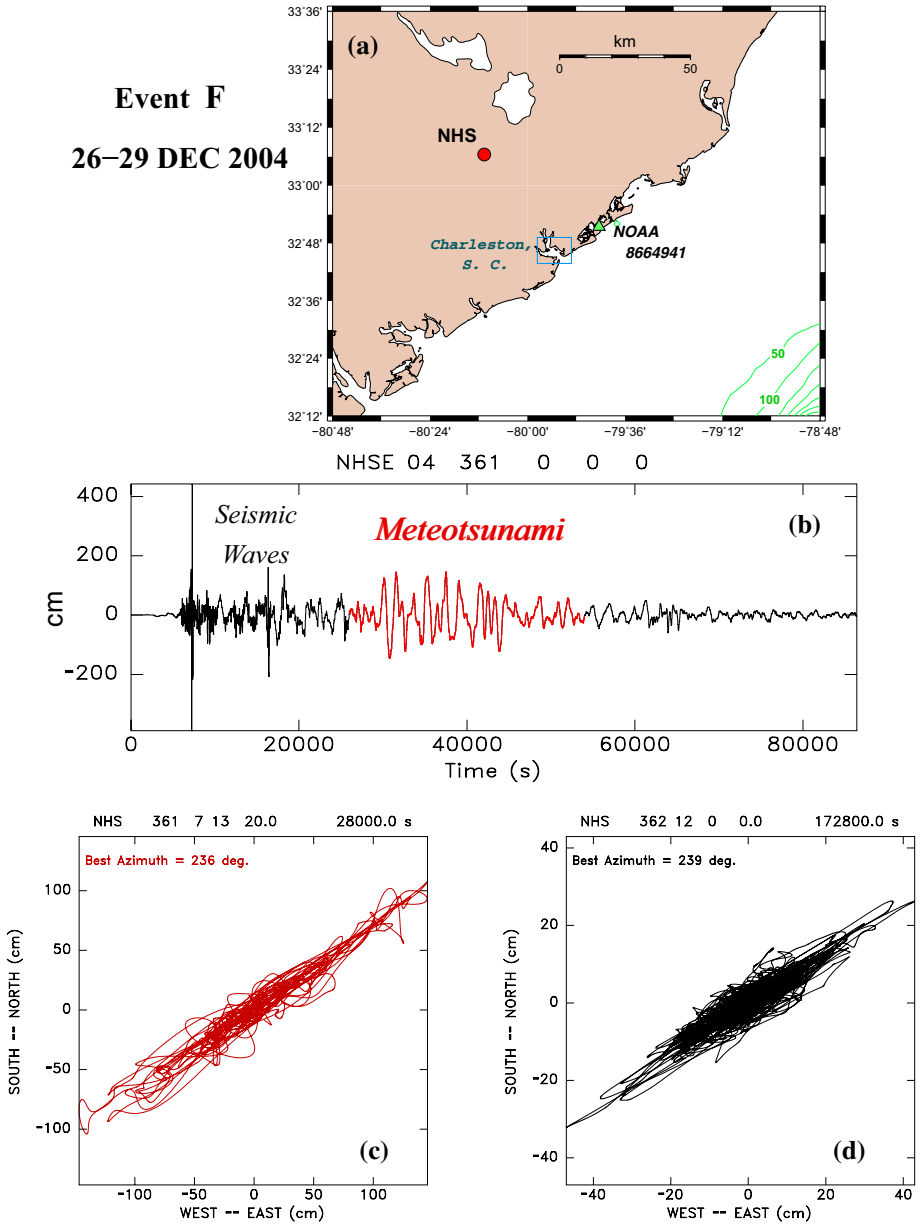

Fig. 11 **a** Location map for Station NHS used in the study of Event **F**. The triangle shows the NOAA tidal gauge station used by Rabinovich and Šepić (2016). The city of Charleston is sketched as the blue square. Isobaths are at 50-m intervals; note the extensive continental shelf. **b** Time series $\eta(t)$ deconvolved from the EW seismogram at NHS, starting at 00:00 on December 26, 1 h before the Sumatra mega-earthquake. The window corresponding to the meteotsunami is outlined in red; the earlier oscillations are the result of deconvolving *GRF* out of the seismic wave train. **c** Horizontal particle motion for the time window plotted in red in (**b**). **d** Same as (**c**) for a time window starting at 00:00 on December 27 (not shown in **b**); note the identical polarization

3.7 Event G: Mostaganem, Algeria, August 03, 2007

We close our selection of events with the tsunami of August 03, 2007, in Mostaganem, Algeria (Fig. 12). On that Friday afternoon, twelve people were killed on local beaches by a sudden wave with an estimated run-up of 7–10 m at Petit Port (Pelinovsky and Kharif 2008). The origin of this phenomenon, which affected a 40-km stretch of coastline (El Watan 2007) but was not reported at other locations in the Mediterranean, has been speculative and controversial.

Amir et al. (2013) suggested that the wave could have resulted from an earthquake located only 19 km away from Petit Port, at 36.24°N, 0.06°E. This event, given a magnitude of $m_b = 5.4$ by the Euro-Mediterranean Seismological Center (EMSC), is too small to generate a tsunami by itself, but it could conceivably have triggered a landslide; larger events are known to have generated tsunamis through this process along the western Algerian coastline, notably in 1954 and 1980 (Heezen and Ewing 1955; Solov'ev et al. 1992). The problem with this interpretation is that the earthquake took place *five days after the tsunami,* on August 08, 2007 at 21:26 GMT, as documented by no fewer than 13 reporting agencies, including the ISC-EHB and ISC-GEM catalogs (Weston et al. 2018; Storchak et al. 2015), the origin of this confusion being probably that the news of the tsunami attack was released by local officials only on Wednesday, August 08. By contrast, no events in the western Mediterranean are known on August 03, although a small earthquake ($M_L = 2.4$) was detected on the *previous day* (August 02, 2007), also at 21:26 GMT (obviously adding to the confusion), but in eastern Algeria, 470 km from Mostaganem and 32 km inland, which rules out any role in the generation of a tsunami, even through an ancillary landslide.

In this context, the possibility remains, at least in principle, of a "silent" landslide triggered by an unreported seismic event. However, an underwater landslide of a volume sufficient to generate a metric tsunami should have been detected as a hydroacoustic signal by the numerous seismic stations in the immediate vicinity of the Mediterranean shorelines; even though the SOFAR channel is less developed than its counterparts in the Pacific, *T* waves have been detected in the Mediterranean following seismic events (e.g., Solarino and Eva 2007; Carmona et al. 2015). We have examined records of the broadband station CART, ideally located in Cartagena, Spain, directly across from Mostaganem, and only 12 km from a shelf sloping steeply into the basin, thus favoring hydroacoustic-to-seismic conversion (Talandier and Okal 1998), but we failed to identify any potential signal on August 03, 2007.

Finally, a number of media including French "reference" newspapers (e.g., Le Figaro 2007; Le Monde 2007) reported speculation that the Mostaganem waves had been generated by the testing of weaponry as part of a secret foreign mission in Algerian waters, even suggesting the implosion of a submarine. Such a scenario remains highly improbable, since a gross order-of-magnitude estimate of the yield necessary to generate a metric tsunami at distances on the order of at least 10 km would approach 1 kt (Mirchina and Pelinovsky 1988); even much smaller explosions are known to give rise to spectacular basin-wide *T* waves (Reymond et al. 2003; Talandier and Okal 2004). In addition, a large implosive source would also have generated strong acoustic waves detectable around the Mediterranean Basin, as evidenced by the case of the *ARA San Juan* (Dall'Osto 2019), and/or classic seismic signals as in the case of the *Kursk* (Koper et al. 2001; Sèbe et al. 2005).

Rather, we explore here the possibility of a meteotsunami to explain the Mostaganem disaster. We were able to document a particularly impressive signal at Cartagena, Spain (CART), only 200 km from Mostaganem (Fig. 13), where it clearly emerges from the

Fig. 12 Event **G**. *Top:* Map of the western Mediterranean Basin, showing the Algerian city of Mostaganem, and the three seismic stations used. The 100-m isobath is shown in green; deeper ones (in blue) are at 500-m intervals. *Bottom:* Close-up of the area affected by flooding on August 03, 2007. The stars indicate the beaches flooded (El Watan 2007). The cities of Mostaganem and Arzew are sketched as squares. Isobaths in meters

background noise in the raw seismograms and lasts on the order of 10 h. In itself, this property is clearly more characteristic of a meteotsunami than of landslide-generated ones. The maximum energy in the seismogram occurs around 11:30 GMT or 12:30 local time (GMT+1), which would be in general agreement with the reports of people being swept on the beaches during the early afternoon. The polarization of the deconvolved wavefield is EW, parallel to the local coastline at CART. In addition, anomalous activity of comparable properties was also recorded at Melilla (MELI) and Mahón (MAHO), with a generally westward propagation of the signal with time. Differences in polarization suggest that the signal recorded at MAHO could be a different response of the Mahón inlet to the same atmospheric system. At Melilla, the signal is polarized NW–SE, generally parallel to the local coastline.

We note that Mostaganem lies on the eastern shore of the Bay of Arzew, which forms an ~40–km crescent on the western Algerian coast, with depths not exceeding 100 m (Fig. 12). In this respect, the dimensions of Arzew Bay are comparable to those of St. Helena Bay, South Africa, in which Okal et al. (2014) successfully modeled the 1969 Dwarskersbos tsunami as a meteorological event.

In summary, our investigations of seismic records at three Spanish stations reveal the presence of signals sharing characteristics with those from documented cases of meteotsunamis, which suggests that an atmospheric disturbance existed in the western Mediterranean Basin on August 03, 2007. It is then proposed that the tragic events at Mostaganem were also derived from that system. We emphasize that the above discussion does not constitute a full modeling of the Mostaganem tsunami, which would require a local atmospheric dataset that remains unavailable. Rather, it argues that, among the several possible sources of this intriguing event, the scenario of a meteotsunami appears most probable.

4 Discussion and Conclusion

We have documented on seven worldwide examples that meteotsunamis are routinely recorded on the horizontal components of land-based seismometers deployed in the vicinity of the affected coastlines. Using the concept of the Gilbert Response Function, $GRF\,(\omega)$, these records can be interpreted quantitatively in terms of an equivalent wave amplitude η in the nearby basin.

In general, our deconvolved amplitudes share the same order of magnitude with available amplitudes reported from the field, e.g., as compiled by Rabinovich (2020), which in itself lends further justification to the process of *GRF* deconvolution introduced by Okal (2007) and Paris et al. (2019). Discrepancies subsist, however, which can be attributed to the different nature of the relevant measurements. For example, a tidal gauge record constitutes a single scientific datum, i.e., the wave amplitude at the sensor; by contrast, a value of η deconvolved from seismograms involves *a priori* a smoothing (or low-pass filtering) of the field over a scale comparable at the very least to the distance between the land-based seismometer and the shoreline and more realistically to the dominant wavelength of the

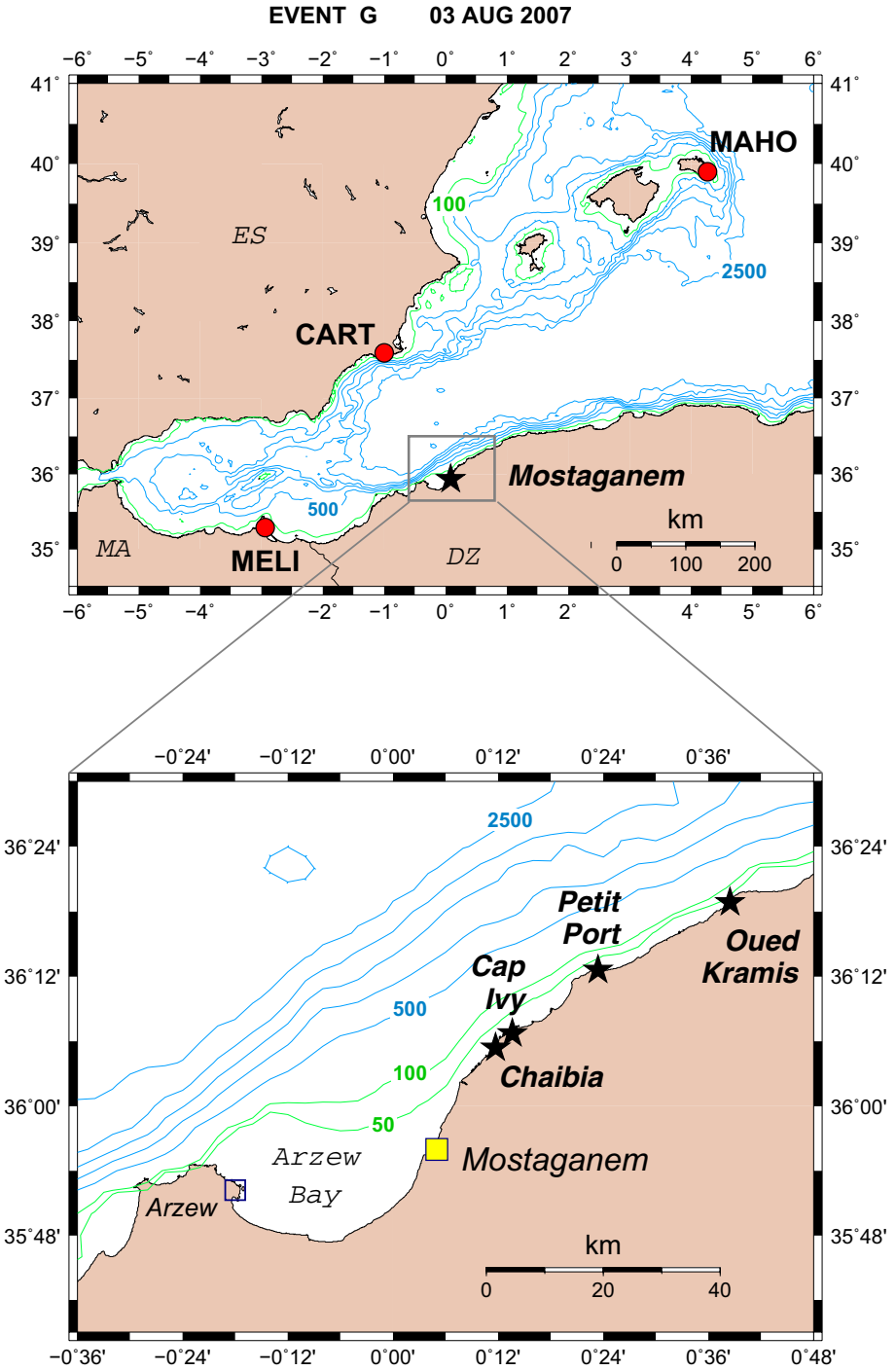
EVENT G 03 AUG 2007
MAHO
CART
MELI
ES
MA
DZ
100
500
2500
Mostaganem
km
0 100 200
Petit Port
Oued Kramis
Cap Ivy
Chaibia
50
Arzew Bay
Arzew
0 20 40

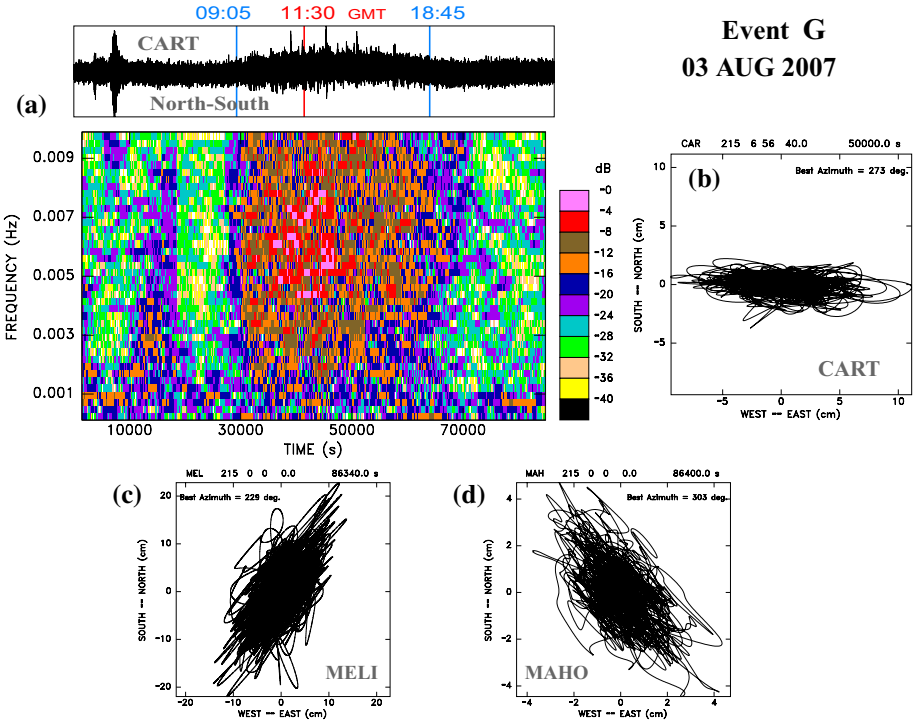

Fig. 13 **a** Raw north–south seismogram at Cartagena and its spectrogram. The window starts at 00:00 GMT on August 03, 2007. The signal at left, ~7000 s into the time series, is from an earthquake south of Australia not contributing to the low-frequency spectrum below 0.01 Hz. **b** Horizontal polarization of deconvolved wave amplitudes for a window starting at 06:56 GMT and lasting 50000 s. **c** Same as (**b**) at Melilla for the whole day, August 03. **d** Same as (**c**) at Mahón

tsunami; as documented in Okal (2007), a station has to be within one wavelength of the tsunami to be able to record it. In addition, tidal gauges, most often located in harbors, are known to suffer from nonlinearity inherent in both their construction and the response of the harbor to an incoming wave. Finally, many of the amplitudes reported, for example, by Rabinovich (2020) consist of non-instrumental estimates gathered by individuals or the media.

In this context, and also given the significant distances between available seismic stations and the locations of reports (e.g., Ciutadella *vs.* Mahón (**A**); Jeju *vs.* Central Korea (**D**)), we chose not to formally compare our results with reported amplitudes.

A remarkable aspect of the deconvolution of seismic records is that it can provide information on the polarization of the tsunami wave, i.e., on the direction of the associated currents. This property was used to investigate the structure of seiching in the Panama Canal by McNamara et al. (2011) and in the Karrat Fjord, Greenland, by Paris et al. (2019). In this respect, recording by seismometer is clearly superior to the measurement of a single amplitude, either by a tidal gauge or by a pressure sensor.

In the majority of our cases, we find a deconvolved field in the direction of the local coastline, which may represent a wave guided by the geometry of the shallow shelf necessary for Proudman resonance. Only in the case of extended shallow structures lacking

a deep basin is the polarization of the wave controlled by the propagation of the parent atmospheric disturbance, as for Event **D** in Korea, in agreement with the findings of Choi et al. (2014), or in Lake Michigan (**E**) where the tsunami keeps the same polarization at beaches oriented differently. Finally, complex structures in the vicinity of the seismic recorder can control the polarization of the wave, as in the case of Mahón Inlet (**A**) and presumably Ston (**B**). In the presence of extremely complex coastlines, the waves can be multipathed, leading to subsequent arrivals of differing polarities (Lesvos, **B**), or in the presence of numerous islands, to the eventual loss of the polarity signal (Incheon, **D**). Note finally that because a meteotsunami is always generated in shallow water, it does not undergo the severe refraction of a deep water wave upon shoaling on a continental shelf, which results in an approach generally perpendicular to the shore.

An additional benefit of seismic data is their much higher sampling rate, which allows the study of water waves beyond the Nyquist frequencies of tidal gauges, and even of DART sensors, whose finer sampling may not be triggered, and the data unavailable in real time, for smaller tsunamis.

On the other hand, the use of seismic records for early warning of meteotsunamis faces the major obstacle that a proper analysis and deconvolution of the Gilbert Response Function require working at very long periods and hence very long time series, which extended over many hours in all the examples studied here. This caveat would significantly diminish their value in the context of the early warning of an impending event. However, an interesting point, illustrated in the case of Event **C** off the Massachusetts coast, is that a seismic station integrates the tsunami field over a sufficiently large distance to occasionally record the beginning of the disturbance before its arrival at the shore, where it can be severely delayed by propagation over extremely shallow waters in the last few km. By the same token, if the meteotsunami is generated in the center of a very large continental shelf, it can then be significantly delayed before it reaches the shelf slope and is recorded by a DART sensor in deep water. Under this combination of conditions, the seismic Station M65A was indeed the first to pick up the meteotsunami, as evidenced in Figs. 5 and 6.

In conclusion, and as mentioned in the introduction, the present study remains of an exploratory nature and is by no means exhaustive. It is probable that seismological archives hold a myriad of similar records, which could prove very useful in the future study of meteotsunamis, in the framework of the mitigation of their hazards to coastal communities.

Acknowledgements I thank the convenors of the First Meteotsunami Conference held in Split in May 2019, especially Dr. Ivica Vilibić for motivating me to write up this contribution. I am grateful to Dr. Nicos Melis and Prof. Tae-Seob Kang for access to the data at Agia Paraskevi and Jeju, respectively. My interest in the Mostaganem tsunami was originally aroused through conversations with Dr. Nasr-Eddine Taibi during a 2010 conference in Zeralda, Algeria. Many figures were drafted using the GMT software (Wessel and Smith 1991). The paper was improved through the comments of two anonymous reviewers.

References

Amir L, Cisternas A, Dudley W, McAdoo B (2013) Coastal impact of tsunami in industrial harbours: study case of the Arzew-Mostaganem region (Western coast of Algeria, North Africa). In: Proceedings of 3rd Specialty Conference Disaster Prevention Mitigation. Montréal, pp DIS-21-1–DIS-21-4

Anderson EJ, Mann GE (2019) Atmospheric and hydrodynamic simulation of a gravity wave induced meteotsunami in Ludington, Michigan. In: The first world conference on meteotsunamis, Split, Croatia, p 36 [abstract]

Bailey K, DiVeglio C, Welty A (2014) An examination of the June 2013 East Coast meteotsunami captured by NOAA observing systems. NOAA Tech. Rept. NOS-CO-OPS 079, 42 pp., U.S. Dept. Commerce, Silver Spring

Bechle AJ, Wu CH (2014) The Lake Michigan meteotsunamis of 1954 revisited. Nat Hazards 74:155–177

Carmona E, Almendros J, Alguacil G, Soto JI, Luzón F, Ibáñez JM (2015) Identification of *T* waves in the Alboran Sea. Pure Appl Geophys 172:3179–3188

Cho K-H, Choi J-Y, Park K-S, Hyun S-K, Oh Y, Park JY (2013) A synoptic study on tsunami-like sea level oscillations along the West coast of Korea using an unstructured-grid ocean model. J Coast Res 65:678–683

Choi B-J, Hwang C, Lee S-H (2014) Meteotsunami-tide interactions and high-frequency sea level oscillations in the Eastern Yellow Sea. J Geophys Res Oceans 119:6725–6742

Dall'Osto RA (2019) Source triangulation utilizing three-dimensional arrivals: application to the search for the ARA San Juan submarine. J Acoust Soc Am 146:2104–2112

Dusek G, DiVeglio C, Licate L, Herman L, Kirk K, Paternostro C, Miller A (2019) A meteotsunami climatology along the U.S. East coast. Bull Am Meteorol Soc 100:1329–1345

Dziewonski AM, Chou TA, Woodhouse JH (1981) Determination of earthquake source parameters from waveform data for studies of global and regional seismicity. J Geophys Res 86:2825–2852

Ekström G, Nettles M, Dziewoński AM (2012) The global CMT project 2004–2010: centroid moment tensors for 13,017 earthquakes. Phys Earth Planet Inter 200:1–9

El Watan, Alger, 11 août 2007

Ewing WM, Press F, Donn WL (1954) An explanation of the Lake Michigan wave of 26 June 1954. Science 120:684–686

Gilbert JF (1980) An introduction to low-frequency seismology. In: Proceedings of international school of physics "Enrico Fermi", Dziewonski AM, Boschi E (eds), vol 78. North Holland, Amsterdam, pp 41–81

Green G (1838) On the motion of waves in a variable canal of small depth and width. Trans Camb Philos Soc 6:457–462

Hanson JA, Bowman JR (2005) Dispersive and reflected tsunami signals from the 2004 Indian Ocean tsunami observed on hydrophones and seismic stations. Geophys Res Lett 32(17):L17606

Heezen BC, Ewing M (1955) Orléansville earthquake and turbidity currents. Am Assoc Petrol Geol Bull 39:2505–2514

Jansà A, Monserrat S, Gomis D (2007) The rissaga of 15 June 2006 in Ciutadella (Menorca): a meteorological tsunami. Adv Geophys 12:1–4

Knight W, Whitmore P, Kim YY, Wang D, Becker N, Weinstein S, Walker K (2013) The U.S. East Coast meteotsunami of June 13, 2013. Eos Trans Am Geophys Un 94:53 NH43A–1740 [abstract]

Koper KD, Wallace TC, Taylor SR, Hartse HE (2001) Forensic seismology and the sinking of the *Kursk*. Eos Trans Am Geophys Un 82:37–45-46

La Rocca M, Galluzzo D, Saccorotti G, Tinti S, Cimini GB, Del Pezzo E (2004) Seismic signals associated with landslides and with a tsunami at Stromboli Volcano, Italy. Bull Seismol Soc Am 94:1850–1867

Le Figaro, Paris, 9 août 2007

Le Monde, Paris, 9 août 2007

McNamara D, Ringler A, Hutt C, Gee L (2011) Seismically observed seiching in the Panama Canal. Phys Res Solid Earth 116(B4):B04312

Mirchina NR, Pelinovsky EN (1988) Estimation of underwater eruption energy based on tsunami wave data. Nat Hazards 1:277–283

Monserrat S, Vilibić I, Rabinovich AB (2006) Meteotsunamis: atmospherically induced destructive ocean waves in the tsunami frequency band. Nat Hazards Earth Syst 6:1035–1051

Okal EA (2007) Seismic records of the 2004 Sumatra and other tsunamis: a quantitative study. Pure Appl Geophys 164:325–353

Okal EA, Visser JNJ, de Beer CH (2014) The Dwarskersbos, South Africa local tsunami of 27 August 1969: Field survey and simulation as a meteorological event. Nat Hazards 74:251–268

Paris A, Okal EA, Guérin C, Heinrich P, Schindelé F, Hébert H (2019) Numerical modeling of the June 17, 2017 landslide and tsunami events in Karrat Fjord, West Greenland. Pure Appl Geophys 176:3035–3057

Pelinovsky E, Kharif C (2008) Preface. In: Extreme ocean waves. Pelinovsky E Kharif C (eds). Springer, Dordrecht

Platzman GW (1958) A numerical computation of the surge of 26 June 1954 on Lake Michigan. Geophysica 6:407–438
Proudman J (1929) The effects on the sea of changes in atmospheric pressure. Mon Not R Astron Soc Geophys Suppl 2:197–209
Rabinovich AB (1997) Spectral analysis of tsunami waves: separation of source and topography effects. J Geophys Res 102:12663–12676
Rabinovich AB (2020) Twenty-seven years of progress in the science of meteorological tsunamis following the 1992 Daytona Beach event. Pure Appl Geophys 177:1193–1230
Rabinovich AB, Šepić J (2016) Meteorological tsunami: what is that? Priroda 1:12–26 [in Russian]
Reymond D, Hyvernaud O, Talandier J, Okal EA (2003) *T*-wave detection of two underwater explosions off Hawaii on April 13, 2000. Bull Seismol Soc Am 93:804–816
Saito M (1967) Excitation of free oscillations and surface waves by a point source in a vertically heterogeneous Earth. J Geophys Res 72:3689–3699
Sèbe O, Bard P-Y, Guilbert J (2005) Single station estimation of seismic source time function from coda waves: The *Kursk* disaster. Geophys Res Lett 32(14):L14308
Šepić J, Rabinovich AB (2014) Meteotsunami in the Great Lakes and on the Atlantic coast of the United States generated by the "derecho" of June 29–30, 2014. Nat Hazards 74:75–107
Šepić J, Vilibić I, Rabinovich A, Monserrat S (2015) Widespread tsunami-like waves of 23–27 June in the Mediterranean and Black Seas generated by high-altitude atmospheric forcing. Sci Rep 5:11682
Solarino S, Eva C (2007) *T* waves in Western Mediterranean Sea after the May 21, 2003 Algerian earthquake. Ann Geophys 50:591–601
Solov'ev SL, Campos-Romero ML, Plink NL (1992) Orléansville tsunami of 1954 and El Asnam tsunami of 1980 in Alboran Sea (Southwestern Mediterranean Sea). Izv Phys Solid Earth 28:739–760
Storchak DA, Di Giacomo D, Engdahl ER, Harris J, Bondár I, Lee WHK, Bormann P, Villaseñor A (2015) The ISC-GEM global instrumental earthquake catalogue (1900–2009): Introduction. Phys Earth Planet Inter 239:48–63
Synolakis CE (1991) Green's law and the evolution of solitary waves. Phys Fluids A 3:490–491
Talandier J, Okal EA (1998) On the mechanism of conversion of seismic waves to and from *T* waves in the vicinity of island shores. Bull Seismol Soc Am 88:621–632
Talandier J, Okal EA (2004) Hydroacoustic signals from presumed CHASE explosions off Vancouver Island in 1969–70: a modern perspective. Seismol Res Lett 75:188–198
Vilibić I, Monserrat S, Rabinovich AB, Mihanović H (2008) Numerical modelling of the destructive meteotsunami of 15 June 2006 on the coast of the Balearic Islands. Pure Appl Geophys 165:2169–2195
Ward SN (1980) Relationships of tsunami generation and an earthquake source. J Phys Earth 28:441–474
Wertman CA, Yablonsky RM, Shen Y, Merrill J, Kincaid CR, Pockalny RA (2014) Mesoscale convective system surface pressure anomalies responsible for meteotsunamis along the U.S. East Coast on June 13th, 2013. Sci Rep 4:7143
Wessel P, Smith WHF (1991) Free software helps map and display data. Eos Trans Am Geophys Un 72:441 and 445−446
Weston J, Engdahl ER, Harris J, Di Giacomo D, Storchak DA (2018) ISC-EHB: reconstruction of a robust earthquake data set. Geophys J Int 214:474–484
Yuan X, Kind R, Pedersen HA (2005) Seismic monitoring of the Indian Ocean tsunami. Geophys Res Lett 32(15):15308